

Work function engineering of MXene contacts for high-performance, self-powered AlGaN solar-blind photodetectors

Pan Dai(代盼), Dengshan Cai(蔡登山), Wenxian Yang(杨文献), Ying Gu(顾颖), Haowen Hua(华浩文), Mengyang Huang(黄梦洋), Peng Zhang(张鹏), Xueyan Feng(冯雪雁), Sijia Wei(魏思嘉), Zheng Zhong(钟政), Yi Gong(龚毅), Jianjun Zhu(朱建军), Shan Jin(金山), Shulong Lu(陆书龙), and Min Jiang(蒋敏)

Citation: Chin. Phys. B, 2026, 35 (**6**): 068503. DOI: 10.1088/1674-1056/ae617d
http://cpb.iphy.ac.cn; http://iopscience.iop.org/cpb

What follows is a list of articles you may be interested in

Degradation mechanisms of Schottky p-GaN gate AlGaN/GaN HEMTs under high-temperature reverse bias stress

Fei Hu(胡飞), Chengbing Pan(潘成兵), Xinyuan Zheng(郑鑫源), Yibo Ning(宁一博), Xueyan Li(李雪燕), and Lixia Zhao(赵丽霞)

Chin. Phys. B, 2025, 34 (**11**): 118501. DOI: 10.1088/1674-1056/ade1c0

Novel double channel reverse conducting GaN HEMT with an integrated MOS-channel diode

Xintong Xie(谢欣桐), Cheng Zhang(张成), Zhijia Zhao(赵智家), Jie Wei(魏杰),Xiaorong Luo(罗小蓉), and Bo Zhang(张波)

Chin. Phys. B, 2023, 32 (**9**): 098506. DOI: 10.1088/1674-1056/ace248

Realization of high-efficiency AlGaN deep ultraviolet light-emitting diodes with polarization-induced doping of the p-AlGaN hole injection layer

Yi-Wei Cao(曹一伟), Quan-Jiang Lv(吕全江), Tian-Peng Yang(杨天鹏), Ting-Ting Mi(米亭亭),Xiao-Wen Wang(王小文), Wei Liu(刘伟), and Jun-Lin Liu(刘军林)

Chin. Phys. B, 2023, 32 (**5**): 058503. DOI: 10.1088/1674-1056/ac9de7

Simulation design of normally-off AlGaN/GaN high-electron-mobility transistors with p-GaN Schottky hybrid gate

Yun-Long He(何云龙), Fang Zhang(张方), Kai Liu(刘凯), Yue-Hua Hong(洪悦华), Xue-Feng Zheng(郑雪峰),Chong Wang(王冲), Xiao-Hua Ma(马晓华), and Yue Hao(郝跃)

Chin. Phys. B, 2022, 31 (**6**): 068501. DOI: 10.1088/1674-1056/ac3739

Current oscillation in GaN-HEMTs with p-GaN islands buried layer for terahertz applications

Wen-Lu Yang(杨文璐), Lin-An Yang(杨林安), Fei-Xiang Shen(申飞翔), Hao Zou(邹浩), Yang Li(李杨), Xiao-Hua Ma(马晓华), and Yue Hao(郝跃)

Chin. Phys. B, 2022, 31 (**5**): 058505. DOI: 10.1088/1674-1056/ac2b1f

---

Work function engineering of MXene contacts for high-performance, self-powered AlGaN solar-blind photodetectors

Pan Dai(代盼)[1], Dengshan Cai(蔡登山)[1], Wenxian Yang(杨文献)[2,†], Ying Gu(顾颖)[2], Haowen Hua(华浩文)[2], Mengyang Huang(黄梦洋)[2], Peng Zhang(张鹏)[2], Xueyan Feng(冯雪雁)[2], Sijia Wei(魏思嘉)[2], Zheng Zhong(钟政)[2], Yi Gong(龚毅)[3], Jianjun Zhu(朱建军)[2], Shan Jin(金山)[2,‡], Shulong Lu(陆书龙)[2], and Min Jiang(蒋敏)[2,§]

[1] *School of Information Engineering, Huzhou University, Huzhou* 213000, *China*

[2] *Key Laboratory of Semiconductor Display Materials and Chips, Suzhou Institute of Nano-Tech and Nano-Bionics, Chinese Academy of Sciences (CAS), Suzhou* 215123, *China*

[3] *College of Future Information Technology, Fudan University, Shanghai* 200433, *China*

(Received 16 March 2026; revised manuscript received 5 April 2026; accepted manuscript online 20 April 2026)

AlGaN-based solar-blind UV photodetectors are crucial for critical applications but suffer from Fermi-level pinning that leads to high dark current. Constructing a high-barrier heterojunction interface effectively suppresses dark current, yet controlling the AlGaN/two-dimensional material barrier via work function modulation remains challenging. Here, we tailor the work function of MXene (3.7–4.6 eV) through surface oxidation to fabricate self-powered MXene/AlGaN van der Waals photodetectors. By alleviating Fermi-level pinning and forming a deep-depletion barrier, the device exhibits a suppression of dark current by nearly four orders of magnitude at 0 V (10^{-14} A regime). Consequently, the device achieves a high responsivity of 15 mA/W and a specific detectivity of 2×10^{11} Jones at 280 nm, accompanied by a rapid response time of 0.66 ms. This work validates work function engineering as a potent strategy for optimizing interface energetics and boosting the performance of wide-bandgap optoelectronics.

Keywords: AlGaN, MXene, solar-blind photodetector, work function engineering, van der Waals heterojunction

PACS: 85.60.Gz, 73.61.Ey, 73.22.–f, 73.30.+y

DOI: 10.1088/1674-1056/ae617d **CSTR:** 32038.14.CPB.ae617d

1. Introduction

Solar-blind photodetectors directly convert DUV light into electrical signals. They play a key role in a wide range of fields, including secure communications, missile warning, neuromorphic vision, and in-sensor computing.[1–4] As a typical ultra-wide bandgap (UWBG) semiconductor, AlGaN is attractive due to its tunable bandgap and mature heteroepitaxial technology, with the metal–semiconductor–metal planar structure being commonly adopted.[5,6] However, the opaque metal electrodes reduce the effective photosensitive area, and more fundamentally, the high density of interface states leads to pronounced Fermi-level pinning.[7] This typically results in a low Schottky barrier height and excessive leakage current, forcing devices to operate under high external bias to achieve efficient carrier separation, which consequently increases power consumption and system complexity.[8–11]

To overcome these fundamental bottlenecks, advanced carrier separation strategies and meticulous interface engineering have recently been demonstrated to be highly effective in UWBG systems, enabling robust, swift, and controllable solar-blind photoresponses.[12,13] Inspired by these successful interfacial engineering concepts, the construction of van der Waals (vdW) heterojunctions by integrating two-dimensional materials with AlGaN has emerged as a promising strategy to address the severe interfacial challenges.[14,15] Among various candidates, MXenes offer distinct advantages over graphene, including high metallic conductivity, optical transparency, rich surface chemistry, and solution processability.[16–19] However, current research on MXene/AlGaN photodetectors predominantly treats MXene merely as a "passive transparent electrode", often neglecting the active modulation of its tunable work function to optimize interfacial band alignment.[20–22] Such unoptimized interfacial barriers not only lead to severe persistent photoconductivity and sluggish response speeds, typically in the tens of milliseconds range, but are also frequently accompanied by elevated dark currents (high noise floor) due to insufficient interface depletion, which critically constrains the signal-to-noise ratio and detection limit.[23–27] Although self-powered operation has been demonstrated, the underlying mechanism for synergistically suppressing dark current and enhancing response kinetics via active barrier height modulation remains under-explored. In particular, the structure-property relationship between MXene work function evolution and heterojunction optoelectronic behavior lacks

[†]Corresponding author. E-mail: wxyang2014@sinano.ac.cn

[‡]Corresponding author. E-mail: sjin2017@sinano.ac.cn

[§]Corresponding author. E-mail: mjiang2020@sinano.ac.cn

© 2026 Chinese Physical Society and IOP Publishing Ltd. All rights, including for text and data mining, AI training, and similar technologies, are reserved.

systematic validation in functional devices.[28,29] To date, strategies employing interfacial barrier engineering to simultaneously achieve high-speed, ultra-low dark current, and self-powered detection have rarely been reported, significantly hindering the full realization of the potential of MXene/AlGaN heterojunctions.

In this work, focusing on the influence of MXene/AlGaN interfacial contact on device performance and its underlying mechanism, we deviate from the conventional "passive electrode" approach and propose a quasi-vertical device architecture centered on active work function engineering.[30,31] Unlike lateral MSM structures, the vertical design maximizes the use of the built-in electric field for efficient carrier separation under zero bias. We synthesized a series of MXene films with controlled surface oxidation levels, enabling systematic tuning of their work functions from 3.7 eV to 4.6 eV. By directly correlating heterojunction height modulation with device metrics, we demonstrate that the suppressed dark current and accelerated response originate from controlled barrier engineering. This work elucidates the physical mechanism of vdW interface engineering and demonstrates a viable pathway toward high-speed, low-noise, and energy-efficient solar-blind photodetection.

2. Results and discussion

2.1. Device design and working mechanism

Figure 1(a) schematically illustrates the quasi-vertical MXene/AlGaN van der Waals heterojunction photodetector. The primary objective of this architecture is to systematically investigate the modulation of the barrier height. Unlike conventional planar metal–semiconductor–metal (MSM) configurations, which are susceptible to surface-state interference and persistent photoconductivity effects, we adopted a quasi-vertical geometry with a mesa etched down to the n-GaN layer.[23,25,32,33] This design serves a dual purpose: first, the heavily doped n-GaN enables a reliable Ohmic contact, acting as a stable reference electrode to eliminate ambiguities associated with the back contact.[26,34] Second, the vertical carrier transport path, confined along the built-in electric field direction, effectively decouples the intrinsic junction behavior from lateral surface leakage.[27] Furthermore, an optimized AlGaN thickness combined with SiO_2 passivation suppresses parasitic surface conduction, thereby ensuring a well-defined junction for accurate characterization.

Figure 1(b) shows the influence of work function tuning on the interfacial energy band alignment. The energy band alignment at the MXene/AlGaN interface after tuning the MXene work function via oxidation is described in detail below. For MXene with a 3.7 eV work function, the relatively high Fermi level leads to minimal band bending and a low barrier height. This is insufficient to suppress thermionic emission, resulting in high leakage current, which is consistent with previous reports on non-optimized vdW contacts.[35,36] As the work function increases to 4.3 eV with enhanced surface oxidation, the downward shift of the Fermi level, driven by the surface dipole of O-terminations, enhances upward band bending and widens the depletion region.[17,37] At a work function of 4.6 eV, a deep-depletion regime is established. The significantly raised barrier not only creates a strong built-in electric field for efficient photocarrier separation but also forms an effective energy barrier that strongly suppresses dark current.[32,38] This progressive band evolution demonstrates that the barrier height is predominantly controlled by tailoring the MXene surface chemistry.

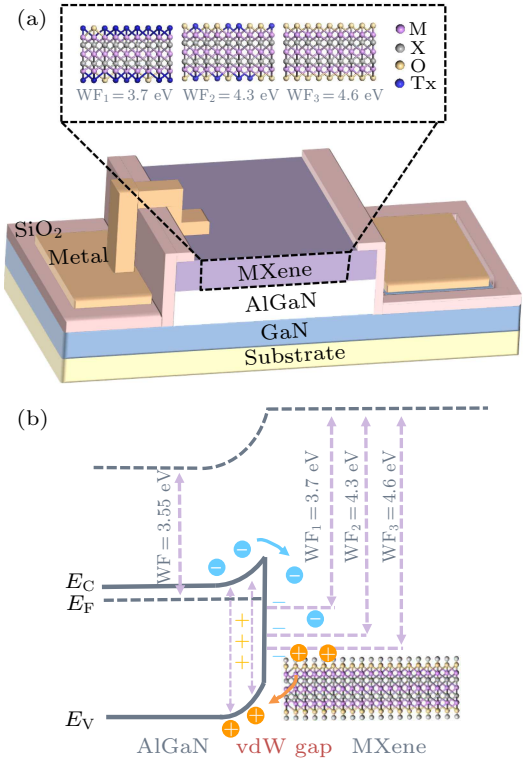


Fig. 1. Schematic of the device structure and interfacial energy-band alignment. (a) Three-dimensional view of the quasi-vertical MXene/AlGaN van der Waals heterojunction photodetector. (b) Corresponding energy-band diagram at equilibrium, illustrating the modulation of the barrier height with MXene work functions (WF_1, WF_2, and WF_3).

2.2. Device fabrication and structural characterization

To confirm the physical realization of the proposed quasi-vertical architecture, Fig. 2(a) shows a detailed microscopic characterization of the device structure. The top-view SEM image, as shown in Fig. 2(b), exhibits a well-defined mesa profile formed by precise ICP etching. The MXene film is confined selectively to the active mesa area, while the unmasked field regions remain clean, demonstrating the high fidelity of the fabrication process in shaping the geometry critical for vertical electric-field distribution.[26,27] Complementing the morphological analysis in Fig. 2(b), energy-dispersive

x-ray spectroscopy (EDS) elemental mapping was conducted. The maps of Ti and O reveal a clear spatial boundary, with both elements concentrated predominantly on the mesa surface. The distinct oxygen signal not only confirms the presence of the MXene layer but also provides direct chemical evidence for the surface-oxidation strategy employed for work-function engineering.[17,37] This confirms that the MXene active layer has undergone the intended chemical modification required to establish the target barrier height. The cross-sectional FIB-SEM image in Fig. 2(c) clearly resolves the vertical layer stack. Despite the nanoscale dimensions, a coherent Metal/MXene/AlGaN/GaN structure is evident. The interfaces show distinct contrast transitions, indicating that the MXene nanofilm is intimately integrated between the top electrode and the AlGaN layer without noticeable interdiffusion or delamination. This structural integrity confirms the successful formation of a robust van der Waals heterojunction, which is essential for minimizing interface states and mitigating Fermi-level pinning.[25,32]

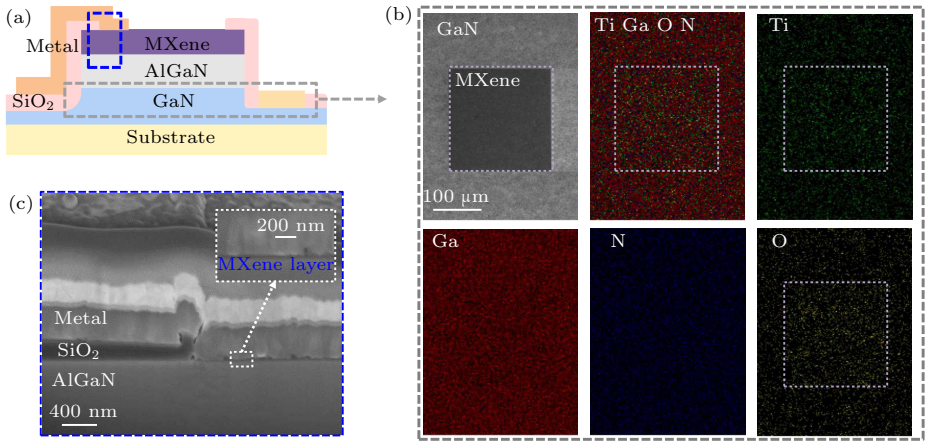


Fig. 2. Structural and compositional characterization of the quasi-vertical MXene/AlGaN photodetector. (a) Schematic of the device architecture. (b) Top-view SEM image of the etched mesa and the corresponding EDS elemental maps of Ti and O overlaid on the SEM image. (c) Cross-sectional FIB-SEM image of the device stack.

2.3. Device fabrication and structural characterization

High-quality constituent materials are essential for high-performance devices. The characteristic (002) peak in the XRD pattern (Fig. S1(a)) confirms successful exfoliation of the phase into 2D MXene nanosheets.[39–41] AFM and SEM characterizations show that the spin-coated MXene film exhibits excellent uniformity. Together with the ultrasmooth AlGaN epitaxial layer in Fig. 3(a), this uniformity establishes a defect-minimized heterojunction interface.[26,27] Subsequent XPS depth profiling in Fig. 3(b) reveals the elemental distribution across the interface. Distinct signals of Al and Ga detected through the MXene layer confirm its ultrathin nature ($\sim$ 10 nm), which facilitates UV transmission. More importantly, the high-resolution Ti 2p spectrum (Fig. 3(c)) indicates a progressive transformation of surface terminations from hydroxyl (OH) to oxygen (O) groups, which is identified as the fundamental mechanism for work-function modulation.[42,43] To quantify the corresponding energy-level shift, as shown in Fig. 3(d), UPS spectra were collected to determine the secondary-electron cutoff.[17,37] Compared with the pristine sample, the oxidized MXene exhibits a pronounced shift toward higher binding energy ($\Delta \approx 0.9$ eV), providing a precise means to tune the barrier height.[29,37,44] In conjunction with UPS results from AlGaN, as shown in Fig. S1(c), a potential barrier difference of $\sim$ 1.0 eV is established, forming the physical basis for effective rectification.[45] Driven by this tunable band alignment, as shown in Fig. 3(e), dark current–voltage (I–V) characteristics of devices incorporating MXene with work functions of 3.7 eV, 4.3 eV, and 4.6 eV were evaluated.[32,34,36] The experimental results indicate that as the MXene work function increases from 3.7 eV to 4.6 eV, the dark current at 0 V is suppressed by nearly four orders of magnitude (from $\sim 10^{-10}$ A down to $\sim 10^{-14}$ A).

It is noteworthy that the forward I–V characteristics exhibit nonideal behavior with an ideality factor $n \gg 2$. Such deviation, commonly observed in wide-bandgap van der Waals heterojunctions, suggests that carrier transport is likely dominated by tunneling or barrier inhomogeneities rather than pure thermionic emission.[35,36] Despite these complex transport kinetics, the most significant finding is the strong correlation between device performance and MXene work function. The drastic suppression of dark current demonstrates that the effective barrier height is modulated by the MXene Fermi level, not pinned by surface states. This highlights the inherent advantage of van der Waals contacts in mitigating Fermi-level pinning.[38] Based on the electrical characterization, Fig. 3(f) illustrates the operating mechanism under UV illumination. The high Schottky barrier formed at the heterointerface effectively blocks electron thermal emission, thereby suppressing dark current. Simultaneously, the strong built-in electric field in the deep depletion region drives efficient separation and collection of photogenerated carriers, ultimately enabling high-performance photodetection.[25]

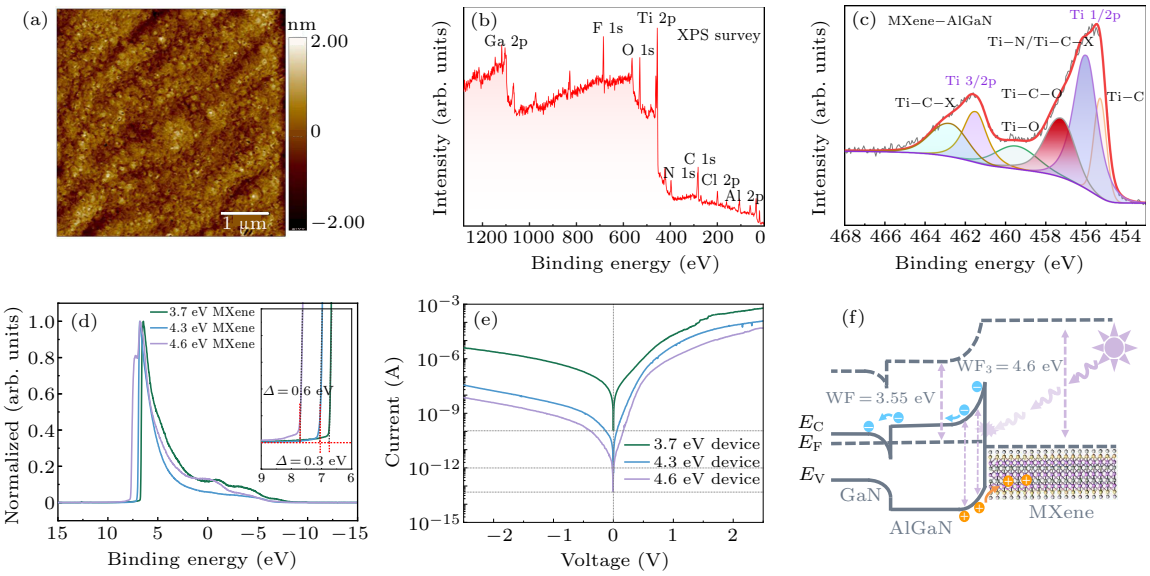


Fig. 3. Material characterization, work-function modulation, and operating mechanism of the MXene/AlGaN photodetector. (a) AFM topography of the epitaxial AlGaN layer. (b) XPS survey spectrum acquired from the MXene/AlGaN heterostructure interface. (c) High-resolution Ti 2p XPS spectrum of the MXene film. (d) UPS spectra showing the secondary-electron cutoff region for work-function extraction. (e) Dark *I*–*V* characteristics of photodetectors fabricated with different MXene electrodes. (f) Schematic energy-band diagram illustrating the carrier-transport mechanism under UV illumination.

2.4. Quantitative evaluation and mechanism analysis of optoelectronic performance

Benefiting from the effective suppression of dark current, the optoelectronic performance of the device was systematically evaluated. The responsivity (R) and specific detectivity (D^*) were calculated from the measured photocurrent (I_{ph}) and dark current (I_{dark}) using standard equations

$$R = (I_{ph} - I_{dark})/P_{inc}, \tag{1}$$

$$D^* = R\sqrt{S}/\sqrt{(2eI_{dark})}, \tag{2}$$

where P_{inc} is the illumination light power. The unoptimized device with 3.7 eV MXene (Fig. S2) exhibited a negligible on/off ratio (< 10) due to the absence of a rectifying barrier, rendering it unsuitable for practical detection. When the work function was increased to 4.3 eV (Fig. S3), marginal improvement was observed, yielding an on/off ratio of 76.9 and a responsivity of 2.8 mA/W. However, the performance remained limited: the insufficient barrier height produced only a weak built-in electric field, which could not efficiently separate carriers against the high dark-current background ($\sim 10^{-12}$), severely limiting the signal-to-noise ratio.[23,25,26]

In contrast, the optimized heterojunction with 4.6 eV MXene demonstrates markedly enhanced performance, confirming the effectiveness of work-function engineering (Figs. 4(a)–4(c)). The device also maintains a wide linear dynamic range (slope ≈ 1, Fig. 4(c)) without saturation.[46,47] Under 0 V bias, the light-to-dark current ratio reaches 756, which is nearly 10 times that of the 4.3 eV device. The responsivity rises to 15 mA/W, a 5.4-fold increase over the 4.3 eV device. Although surface oxidation introduces some series resistance, the dominant benefit of barrier-enhanced carrier collection results in a net performance gain. Spectral responsivity (Fig. S4) further confirms excellent solar-blind selectivity, with a pronounced peak at 280 nm and a sharp cutoff toward the visible region, indicating a high UV-to-visible rejection ratio. The simultaneously elevated barrier height suppresses dark current by nearly four orders of magnitude. This yields a specific detectivity (D^*) of 2×10^{11} Jones within the solar-blind band, while D^* remains negligible in the visible range, ensuring high detection fidelity.

Most importantly, as shown in Figs. 4(e) and 4(f), the device exhibits a fast self-powered response, with a rise time of 0.66 ms and a decay time of 4.6 ms. As summarized in Table 1, this temporal performance surpasses that of recent planar MXene-based (21 ms) and graphene-based (100 ms) AlGaN photodetectors by orders of magnitude. Additionally, the device realizes an ultra-low dark current of $\approx 10^{-14}$ A, representing a substantial improvement in noise suppression. The exceptional speed and low leakage are attributed directly to the quasi-vertical architecture: (1) the quasi-vertical geometry shortens the carrier transit path compared with lateral MSM structures, and (2) the strong built-in electric field, engineered via work-function tuning, ensures efficient carrier sweep-out before recombination while effectively blocking interfacial thermal emission, thus mitigating persistent photoconductivity.[23,26] In summary, the tunable MXene/AlGaN contact interface enables low dark current and fast response speed, demonstrating significant potential for high signal-to-noise ratio and high-speed signal detection applications.

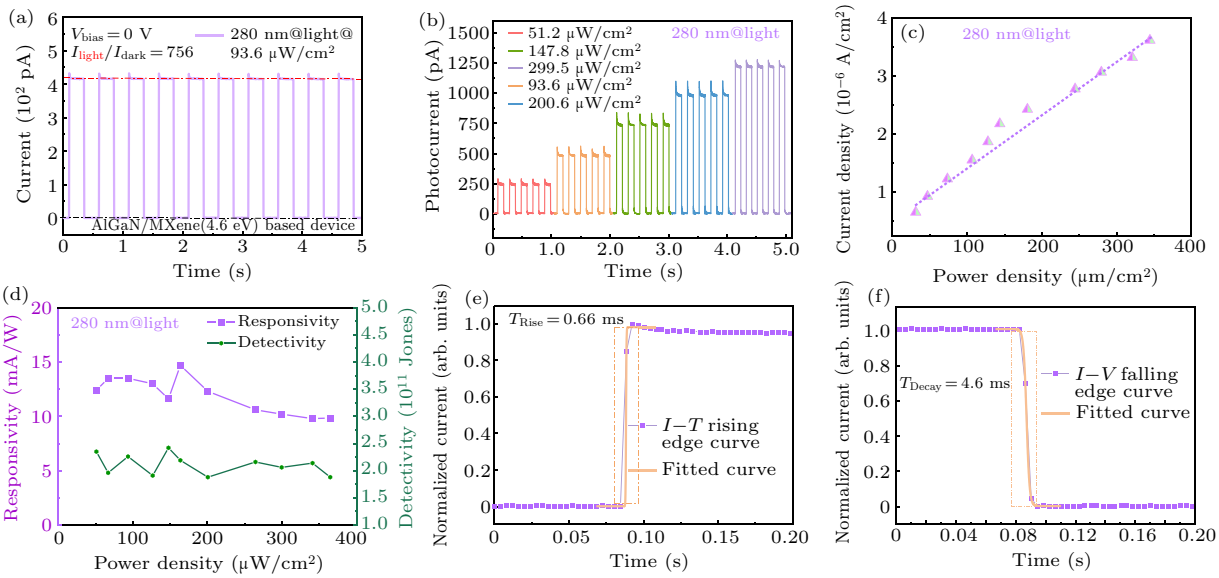


Fig. 4. Optoelectronic performance of the optimized photodetector employing MXene with a work function of 4.6 eV. (a) Temporal photoresponse (I–T) at 0 V bias under 280 nm illumination. (b) Normalized transient response under different optical power densities. (c) Photocurrent as a function of incident optical power. The solid line is a linear fit. (d) Responsivity and specific detectivity versus optical power. Enlarged view of a single cycle showing the (e) rise and (f) decay times.

Table 1. Performance comparison of this work with other reported AlGaN-based heterojunction devices.

Devices structure	Wavelength (nm)	Dark current (A)	Rise/decay time (ms)	Reference
$Ti_3C_2T_x$/AlGaN	280	10^{-14} (0 V)	0.66/4.6	this work
Pd@Nb_2CT_x/AlGaN	254	10^{-10} (0 V)	37.8/14.5	[48]
Al NPs/AlGaN	288	10^{-13} (0 V)	/	[49]
Nb_2CT_x/AlGaN	254	10^{-11} (0 V)	21/22	[20]
$Ti_3C_2T_{x/}$AlGaN	270	10^{-10} (0 V)	72/30	[21]
Graphene/AlGaN /GaN	300	10^{-13} (0 V)	100/13700	[50]

3. Conclusion

In summary, we have demonstrated a surface-chemistry-driven work-function engineering strategy to optimize self-powered MXene/AlGaN solar-blind UV photodetectors. Using a quasi-vertical architecture as a physical platform, we directly show that increasing the MXene work function to 4.6 eV effectively drives the interface into a deep-depletion regime. The optimized device simultaneously achieves an ultralow dark current ($\sim 10^{-14}$ A), a high specific detectivity of 2×10^{11} Jones, and a fast response time of 0.66 ms at 0 V bias. These results clarify the mechanism of barrier modulation at 2D/3D interfaces and establish MXene-based quasi-vertical heterojunctions as promising candidates for high-speed, energy-efficient wide-bandgap optoelectronics. While surface oxidation enables effective work-function tuning, its detrimental impact on MXene conductivity and interfacial stability remains a critical challenge. Encapsulation strategies or alternative electrode engineering will be essential to ensure long-term reliability, unlocking the full potential of MXene-based solar-blind photodetectors.

Appendix A: Methods

A1. Epitaxial growth of AlGaN epilayers

AlGaN epitaxial layers were grown on a 3-μm-thick GaN-on-sapphire template using a Veeco GEN 20 A radio-frequency plasma-assisted molecular beam epitaxy (PA-MBE) system. Prior to growth, the substrate was thermally cleaned at 850 °C under ultra-high vacuum. The AlGaN layer was then deposited at a substrate temperature of 780 °C, with an Al flux calibrated to achieve a target Al composition of $x \approx 0.2$. The growth was monitored in situ by reflection high-energy electron diffraction (RHEED).

A2. Synthesis of $Ti_3C_2T_x$ MXene solution

Few-layer $Ti_3C_2T_x$ MXene was synthesized by selectively etching the Al layer from the $Ti_3C_2T_x$ phase using a LiF/HCl solution, followed by delamination via mild sonication, as detailed in our previous work.[39–41] The resulting colloidal suspension was centrifuged and washed repeatedly with deionized water until the supernatant reached a pH > 6. The final solution was vacuum-sealed and stored at 4 °C to minimize oxidation.

To actively engineer the MXene work function (from 3.7 eV to 4.6 eV), a controlled surface oxidation process was

employed. The colloidal solution was aged in a sealed chamber under an O_2 atmosphere at room temperature. The oxidation level was precisely tuned by the exposure time: freshly prepared (< 24 h) for the 3.7 eV state, 48 h for 4.3 eV, and 96 h for 4.6 eV. To remove any trace particulates or aggregates inevitably formed during prolonged oxidation, the aged solutions were centrifuged. Only the purified supernatant was extracted for subsequent spin-coating and XPS/UPS characterizations, ensuring a high-quality, defect-minimized heterojunction interface. The oxidation of MXene is initiated by nucleophilic attack of water molecules on surface titanium atoms, during which Ti atoms lose electrons (oxidation) while water molecules are reduced.[51] Meanwhile, dissolved oxygen acts as a strong oxidant that further extracts electrons from Ti atoms, accelerating the evolution of surface functional groups and enabling work function tuning.[52,53]

A3. Device fabrication

The fabrication process began with rigorous substrate cleaning. The AlGaN epiwafer was ultrasonically cleaned in acetone and isopropanol, followed by immersion in a piranha solution (H_2SO_4:H_2O_2) for 10 min to remove organic residues and native oxides. After rinsing with deionized water and N_2 drying, the $Ti_3C_2T_x$ solution was spin-coated onto the surface at 3000 rpm for 30 s and annealed at 150 °C in air for 10 minutes. Device mesas (200 × 200 μm) were defined by standard photolithography and etched using an inductively coupled plasma (ICP-180) system with a Cl_2/BCl_3 gas mixture, stopping at the n-GaN layer. A 100-nm-thick SiO_2 passivation layer was then deposited by plasma-enhanced chemical vapor deposition (PECVD). Finally, Ti/Au (20/100 nm) electrodes were deposited by electron-beam evaporation (EI-5Z) and patterned via lift-off to complete the quasi-vertical heterojunction.

A4. Characterization and measurements

The crystal structure was analyzed by x-ray diffraction (XRD, Rigaku SmartLab). Surface morphology was characterized by atomic force microscopy (AFM, Bruker Dimension Icon) and scanning electron microscopy (SEM, Hitachi SU5000). Chemical states and work functions were determined by x-ray photoelectron spectroscopy (XPS, Thermo Scientific K-Alpha) and ultraviolet photoelectron spectroscopy (UPS, He I radiation, 21.2 eV), respectively. Electrical characteristics (I–V and I–T) were measured using a semiconductor parameter analyzer (Keysight B1500A) under dark and illuminated conditions in a probe station. Optoelectronic performance was evaluated using a calibrated 280 nm UV LED as the light source, with optical power adjusted by neutral density filters and measured by a standard silicon photodiode (Newport 1918-C).

Acknowledgements

This work was supported by the National Key Research and Development Program (Grant No. 2023YFB3609800), the National Natural Science Foundation of China (Grant No. 62304244), China Postdoctoral Science Foundation (Grant No. 2025M780550), Frontier Technologies R&D Program of Jiangsu (Grant No. BF2025032), the Natural Science Foundation of Jiangsu (Grant No. BK20230235), the Suzhou Key Core Technology Project: Leading the Charge with Open Competition (Grant No. SYG2024104), the Welfare Applied Research Project of Huzhou (Grant No. 2025GY009), and the "Eagle Fund" Student Original Research Project of the USTC (Grant No. XY2025G002). We are grateful to the technical support from Vacuum Interconnected Nanotech Workstation (Nano-X), Nanofabrication Facility (SNFF), and Platform for Characterization & Test from Suzhou Institute of Nano-Tech and Nano-Bionics (SINANO), Chinese Academy of Sciences (CAS).

References

[1] Monroy E, Calle F, Pau J L, Muñoz E, Omnès F, Beaumont B and Gibart P 2001 *J. Cryst. Growth* **230** 537
[2] Cai Q, You H, Guo H, Wang J, Liu B, Xie Z, Chen D, Lu H, Zheng Y and Zhang R 2021 *Light-Sci. Appl.* **10** 94
[3] Hou X, Li C, Chen C, Bai S, liu Y, Peng Z, Zhao X, Zhou X, Xu G, Gao N and Long S 2025 *Adv. Mater.* **37** 2506179
[4] Zou Y, Liu Y, Zhao X, Wang Y, Xin Y, Zhan H, Feng X, Yu S, Ding W, Fu Z, Hou X and Long S 2025 *ACS Nano* **19** 30823
[5] Huan Z, Lv Q, Yu M, Li R, Huang Z, Liu G, Qiao G and Liu J 2024 *Sens. Actuator A-Phys.* **370** 115254
[6] Maraj M, Li Y Z and Sun W H 2025 *J. Lumin.* **281** 121178
[7] Sun X, Wang D, Wu X, Zhang J, Lin Y, Luo D, Li F, Zhang H, Chen W, Liu X, Kang Y, Yu H, Luo Y, Ge B and Sun H 2024 *Sci. Bull.* **69** 3692
[8] Abutawahina M S M, Mohammed A A A, Hamzah N A, Ng S S, Quah H J, Ahmed N M and Shaveisi M 2024 *Sens. Actuator A-Phys.* **380** 116058
[9] Kim Y J, Kumar M R, Kumar G M and Kim M 2023 *Appl. Phys. Lett.* **123** 252111
[10] Ozbey D H, Sargin G O, Ongun Ozcelik V and Durgun E 2025 *J. Appl. Phys.* **138** 084304
[11] Zheng G, Zhang R, Wang Y, Hou Q, Li M, Xiao K, Deng J and Sun W 2023 *Micro Nanostructures* **184** 207680
[12] Wang Y L, Wu W T,Han K J, Zhan H Y, Huang S Y, Tong P W, Zhao X L,Liu J L, Feng X, Hou X H,Huang H, Wang W, Xu G W, Zhou X Z and Long S B 2025 *IEEE IEDM.*
[13] Wang Z, Han K, Huang H, Zhao X, Zhan H, Hou X, Feng X, Zhou X, Xu G, Zhang F and Long S 2024 *Adv. Funct. Mater.* **34** 2400498
[14] Sun G, Li W, Wan P, Xu T, Zhai Y, Luan C, Zhou Y, Kan C, Shi D and Jiang M 2025 *Appl. Phys. Lett.* **127** 011101
[15] Yue Y, Chen Y, Jiang J, Wang H, Zhang S, Jia Y, Jiang K, Sun X and Li D 2024 *Photon. Res.* **12** 1858
[16] Hart J L, Hantanasirisakul K, Lang A C, Anasori B, Pinto D, Pivak Y, van Omme J T, May S J, Gogotsi Y and Taheri M L 2019 *Nat. Commun.* **10** 522
[17] Schultz T, Frey N C, Hantanasirisakul K, Park S, May S J, Shenoy V B, Gogotsi Y and Koch N 2019 *Chem. Mater.* **31** 6590
[18] Ahn S, Han T H, Maleski K, Song J, Kim Y H, Park M H, Zhou H, Yoo S, Gogotsi Y and Lee T W 2020 *Adv. Mater.* **32** 2000919
[19] Bai L N, Kong L Y, Wen J, Ma N, Gao H and Zhang X T 2020 *Chin. Phys. B* **29** 016802
[20] Li L H, He Y X, Lin T J, Jiang H S, Li Y, Lin T T, Zhou C J, Li G Q and Wang W L 2024 *Appl. Phys. Lett.* **124** 132105

[21] Yü J, Zhang Y, Wang L, Yang X, Yang Y, Jiang K, Lü W and Sun X 2024 *Ionics* **30** 1785
[22] Montazeri K, Currie M, Verger L, Dianat P, Barsoum M W and Nabet B 2019 *Adv. Mater.* **31** 1903271
[23] Ding Y, Xu X M, Zhuang Z, Sang Y M, Cui M, Li W X, Yan Y, Tao T, Xu W Z, Ren F F, Ye J D, Chen D J, Lu H, Zhang R, Alshareef H N and Liu B 2024 *Appl. Phys. Rev.* **11** 041413
[24] Kong D Q, Lin T T, Chai J X, Zhu Z H, Liu P X, Lin Z L, Lin T J, Li L H, Chen L, Li G Q and Wang W L 2023 *Appl. Phys. Lett.* **122** 142104
[25] Luo L Z, Huang Y X, Cheng K M, Alhassan A, Alqahtani M, Tang L B, Wang Z M and Wu J 2021 *Light-Sci. Appl.* **10** 177
[26] Song W, Chen J, Li Z and Fang X 2021 *Adv. Mater.* **33** 2101059
[27] Yi C J, Chen Y B, Kang Z, Ma Y A, Yue Y, Liu W J, Zhu M and Gao Y H 2021 *Adv. Electron. Mater.* **7** 2000955
[28] Ayodhya D 2023 *Diam. Relat. Mat.* **132** 109634
[29] Roy P, Rekhi L, Koh S W, Li H and Choksi T S 2023 *J. Phys-Energy.* **5** 034005
[30] Wang Q, Wang T, Pu T, Cheng S, Li X, Li L and Ao J 2022 *Chin. Phys. B* **31** 057702
[31] Chang Q, Hou B, Yang L, Wu M, Zhang M, Lu H, Jia F, Niu X, Shi C, Du J, Jia M, Yu Q, Li S, Zhu Y, Ma X and Hao Y 2024 *Sci. China-Inf. Sci.* **67** 229402
[32] Liu Y Y, Strandins P and Wei S H 2016 *Sci. Adv.* **2** 1600069
[33] Zhang X W, Shao J H, Yan C X, Wang X M, Wang Y F, Lu Z H, Qin R J, Huang X W, Tian J L and Zeng L H 2021 *Mater. Design.* **207** 109850
[34] Wang C J, Xu X M, Tyagi S, Rout P C, Schwingenschlögl U, Sarkar B, Khandelwal V, Liu X K, Gao L F, Hedhili M N, Alshareef H N and Li X H 2023 *Adv. Mater.* **35** 2211738
[35] Wu Y H, Lou J C, Zhang J, He Z C, Lan Y, Huang G F, Hu W Y and Huang W Q 2023 *Res. Phys.* **54** 107047
[36] Liu Y Y, Xiao H and Goddard W A 2016 *J. Am. Chem. Soc.* **138** 15853
[37] Agresti A, Pazniak A, Pescetelli S, Di Vito A, Rossi D, Pecchia A, Auf der Maur M, Liedl A, Larciprete R, Kuznetsov D V, Saranin D and Di Carlo A 2019 *Nat. Mater.* **18** 1228
[38] Purbayanto M A K, Chandel M, Birowska M, Rosenkranz A and Jastrzebska A M 2023 *Adv. Mater.* **35** 2301850
[39] Alhabeb M, Maleski K, Anasori B, Lelyukh P, Clark L, Sin S and Gogotsi Y 2017 *Chem. Mater.* **29** 7633
[40] Naguib M, Mashtalir O, Carle J, Presser V, Lu J, Hultman L, Gogotsi Y and Barsoum M W 2012 *ACS Nano.* **6** 1322
[41] Naguib M, Mochalin V N, Barsoum M W and Gogotsi Y 2014 *Adv. Mater.* **26** 992
[42] Halim J, Cook K M, Naguib M, Eklund P, Gogotsi Y, Rosen J and Barsoum M W 2016 *Appl. Surf. Sci.* **362** 406
[43] Näslund L Å, Persson P O Å and Rosen J 2020 *Phys. Chem. C* **124** 27732
[44] Yang L L, Peng Y S, Liu Z, Zhang M L, Guo Y F, Yang Y and Tang W H 2023 *Chin. Phys. B* **32** 047301
[45] Jiang C, Lu H, Chen D J, Ren F F, Zhang R and Zheng Y D 2014 *Chin. Phys. B* **23** 097308
[46] Liu Z, Du L, Zhang S H, Li L, Xi Z Y, Tang J C, Fang J P, Zhang M L, Yang L L, Li S, Li P G, Guo Y F and Tang W H 2022 *IEEE Trans. Electron Devices* **69** 5595
[47] Prasad C V, Labed M, Park J H, Kim K J and Rim Y S 2024 *Mater. Today Phys.* **40** 101327
[48] He Y, Li L, Chen J, Wang Y, Li G and Wang W 2024 *Appl. Phys. Lett.* **125** 122101
[49] Wu Y, Sun X, Shi Z, Jia Y, Jiang K, Ben J, Kai C, Wang Y, Lü W and Li D 2020 *Nanoscale Adv.* **2** 1854
[50] Kumar M, Jeong H, Polat K, Okyay A K and Lee D 2016 *J. Phys. D-Appl. Phys.* **49** 275105
[51] Tian Y, Hou P, Zhang H, Xie Y, Chen G, Li Q, Du F, Vojvodic A, Wu J and Meng X 2024 *Nat. Commun.* **15** 10099
[52] Stratulat A M, Nesterova V, Korostelev V, Beidaghi M, Mochalin V and Klyukin K 2025 *ACS Nano* **19** 36994
[53] Huang S and Mochalin V N 2020 *ACS Nano* **14** 10251